



Article

Analysis of Storage Capacity Change and Dam Failure Risk for Tailings Ponds Using WebGIS-Based UAV 3D Image

Meihong Zhi ¹, Yun Zhu ^{1,*}, Ji-Cheng Jang ¹, Shuxiao Wang ², Pen-Chi Chiang ^{3,4}, Chuang Su ⁵, Shenglun Liang ⁶, Ying Li ⁷ and Yingzhi Yuan ¹

¹ College of Environment and Energy, South China University of Technology, Guangzhou Higher Education Mega Center, Guangzhou 510006, China

² State Key Joint Laboratory of Environment Simulation and Pollution Control, School of Environment, Tsinghua University, Beijing 100084, China

³ Graduate Institute of Environmental Engineering, National Taiwan University, Taipei 10673, Taiwan

⁴ Carbon Cycle Research Center, National Taiwan University, Taipei 10672, Taiwan

⁵ Solid Waste and Chemicals Environmental Center of Guangdong Province, Guangzhou 510308, China

⁶ Cloud Information and Environmental Science Technology Company Limited, Foshan 528300, China

⁷ Center for Satellite Application on Ecology and Environment, Ministry of Ecology and Environment, Beijing 100094, China

* Correspondence: zhuyun@scut.edu.cn; Tel.: +86-13316253667



Citation: Zhi, M.; Zhu, Y.; Jang, J.-C.; Wang, S.; Chiang, P.-C.; Su, C.; Liang, S.; Li, Y.; Yuan, Y. Analysis of Storage Capacity Change and Dam Failure Risk for Tailings Ponds Using WebGIS-Based UAV 3D Image. *Sustainability* **2023**, *15*, 14062. <https://doi.org/10.3390/su151914062>

Academic Editors: Hao Sun, Jinbao Jiang, Peng Hou and Yuebin Wang

Received: 7 August 2023

Revised: 1 September 2023

Accepted: 20 September 2023

Published: 22 September 2023



Copyright: © 2023 by the authors. Licensee MDPI, Basel, Switzerland. This article is an open access article distributed under the terms and conditions of the Creative Commons Attribution (CC BY) license (<https://creativecommons.org/licenses/by/4.0/>).

1. Introduction

Tailings ponds are an indispensable facility for mining operations [1], which are also a potential hazard source of man-made mudslides with high potential energy [2,3]. If a tailings dam breaks, it could result in severe damage to the downstream area, including loss of life, property damage, and ecological harm [4–9]. Due to the limited technical measures for the tailings pond's supervision, tailings dam failures with potential environmental safety hazards have occurred occasionally in recent years all over the world [10–13]. Among these, overtopping is the most frequent cause of tailings dam failure [14,15], with its principal inciting factor being attributed to heavy rainfall [16,17]. As a result, the Ministry of Ecology and Environment has mandated at least one comprehensive pollution hazard inspection of

tailings ponds before the annual flood season. Furthermore, the integration of unmanned aerial vehicles (UAVs) and other advanced technologies has been advocated to bolster effective safety surveillance. The efficient application of UAV technology in dynamically analyzing storage capacity change and dam failure risk for tailings ponds has become one of the imperative research fields.

The conventional methods employed for safety monitoring of tailings ponds mostly rely on a combination of manual operation of total station measurement and sensor monitoring, which could be not only time-consuming, laborious, and costly, but also subject to a range of factors such as weather and site conditions [18,19]. In an effort to address these challenges, researchers such as Martinez-Segura et al. [20], Martin-Velazquez et al. [21], and Martin-Crespo et al. [22] have turned to newly merged 3D LiDAR technology to estimate mining and tailings pond volumes, but the high cost may prohibit this technology from its widespread application in tailings ponds [23]. On the other hand, unmanned aerial vehicle oblique photography (UAVOP) has become prevalent in various fields [24–26] because of its advantages of timeliness, flexibility, and relatively low overall cost [27,28], enabling relatively accurate representation of model texture features and the acquisition of spatial 3D data [29]. Correspondingly, the research on the applications of UAVOP technology in tailings ponds and mines has drawn significant attention as well [30–36]. For instance, Wang et al. [31] presented a multidisciplinary approach combining UAV photogrammetry and a smoothed particle hydrodynamics (SPH) numerical method to model potential tailings dam breach overland flow, demonstrating that high-precision DSM data from UAVOP could enhance the accuracy of such simulations. Melton et al. [34] used a UAV-photogrammetrically derived point cloud to estimate volume and area of tailing stockpiles and further detected possible distribution changes of Pb contamination in and around the city of Cerro de Pasco, Peru using a spectral angle mapper. Zhang et al. [36] presented a comprehensive approach for tailings pond risk identification using UAV oblique photography and an integrated space–sky–earth system, with the aim of using UAV 3D images for the observation of surface details of tailings ponds. Notably, these prior studies were mainly focused on using UAVOP technology for surface detail observation, subsidence sensor monitoring and simulations of post-dam failure scenarios in terms of scope, hazards, etc. However, there were limited studies on the utilization of UAVOP for the evaluation of storage capacity change and the risk analysis of flood overtopping prior to dam failure of tailings ponds. Particularly noteworthy is the paucity of exploration into the amalgamation of UAV 3D imagery with WebGIS-based volume measurement and flood regulation calculation within this domain.

This study embarked on the construction of realistic 3D images of a tailings pond located in Guangdong Province, China, employing the Unmanned Aerial Vehicle Oblique Photography (UAVOP) approach. Subsequently, the resulting 3D images were harnessed within the WebGIS framework to implement the visualization and volume measurement of the tailings pond. Finally, the storage capacity change in the tailings pond at different observation times was evaluated and the dam overtopping failure parameters were measured and analyzed in conjunction with the calculation of flood regulation storage capacity. The success of this study should be valuable for grasping the safety condition of the tailings pond and further providing critical data and technical support for its dam failure risk assessment as well as the design of control measures.

2. Materials and Methods

The flow diagram of this study is shown in Figure 1. First, the image control points were placed and measured within and around the tailings pond, and the UAV, equipped with a 5-angle camera, was used to capture high-resolution 5-angle photos of the tailings pond. Second, the photos were preprocessed using Agisoft Metashape software version 1.5.4 [37,38] to obtain the aerotriangulation blocks. The aforementioned blocks, together with the control point data, were then imported into Bentley ContextCapture software version 4.4.12 [39,40] for 3D modeling, outputting 3D real-scene images of the

tailings pond. The accuracy of these 3D images was validated using checkpoint data. Next, WebGIS [41] technology was utilized to visualize the 3D images of the tailings pond, including functions such as publishing 3D images, spatial geometry measurement, and volume change measurement by the square grid method. Finally, the WebGIS visualization analysis function was leveraged to measure the storage capacity change in the tailings pond during different aerial photography periods. Combined with the calculation of flood regulation storage capacity, the minimum flood control dam width, minimum free height, and dam slope ratio were measured on the 3D images to analyze the compliance with dam failure risk parameters of the tailings pond.

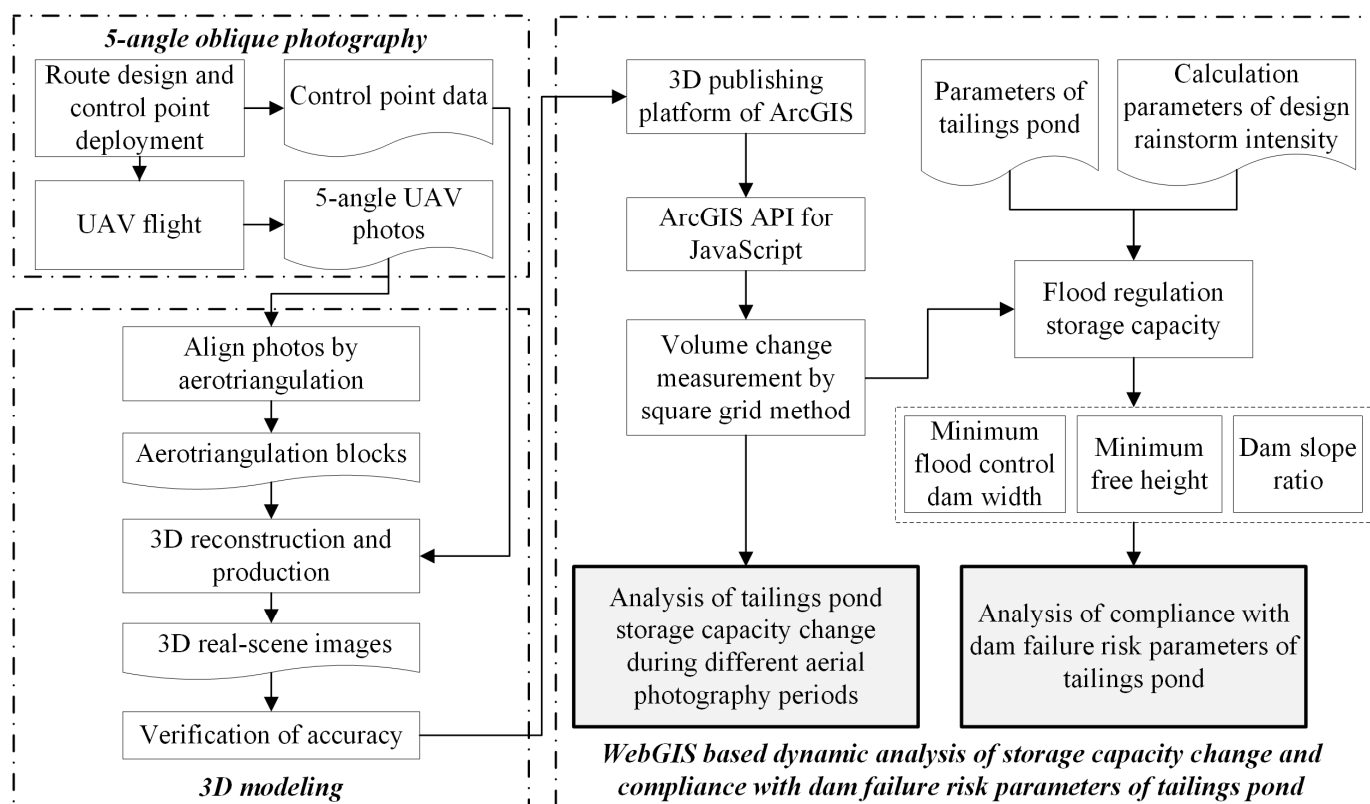


Figure 1. Flow diagram of the analysis of the storage capacity change and dam failure risk for tailings ponds using WebGIS-based UAV 3D images.

2.1. Study Area

Illustrated in Figure 2, the study area pertains to a tailings pond located in Yunan District, Yunfu City, Guangdong Province, Southern China. This region is situated between $111^{\circ}43'26''$ – $112^{\circ}10'17''$ E and $22^{\circ}34'26''$ – $23^{\circ}08'01''$ N. Characterized by hilly land, rich in mountainous, hydraulic, and mineral resources, Yunan District hosts prominent mineral deposits such as lead-zinc, tin, iron, silver, and limestone ores. The locality falls within the lateritic red soil belt of the southern subtropical monsoon forest, primarily featuring lateritic red, red, and yellow soils. Geological formations mainly encompass calcareous rock, banded marble, and siliceous limestone. Climatically, the area lies within the southern subtropical-monsoonal zone, experiencing a warm and humid environment with substantial rainfall. The indigenous vegetation is characterized as lower subtropical evergreen broadleaved forest, boasting a diverse array of more than 600 plant species across 130 families and 369 genera [42,43].

The mining site hosting the tailings pond covers an area of 5.5238 km^2 , primarily focusing on the extraction of zinc, lead, and silver ores, contributing to an annual production of 330,000 tons. This tailings pond is in a dry-stack approach with a typical and common configuration of valley-type and upstream-embankment. Remarkably, the up-

stream method has been notably prevalent in the construction of numerous past tailings dams particularly within China, but which is now considered the least stable among the tailings dam construction approaches [15,44].

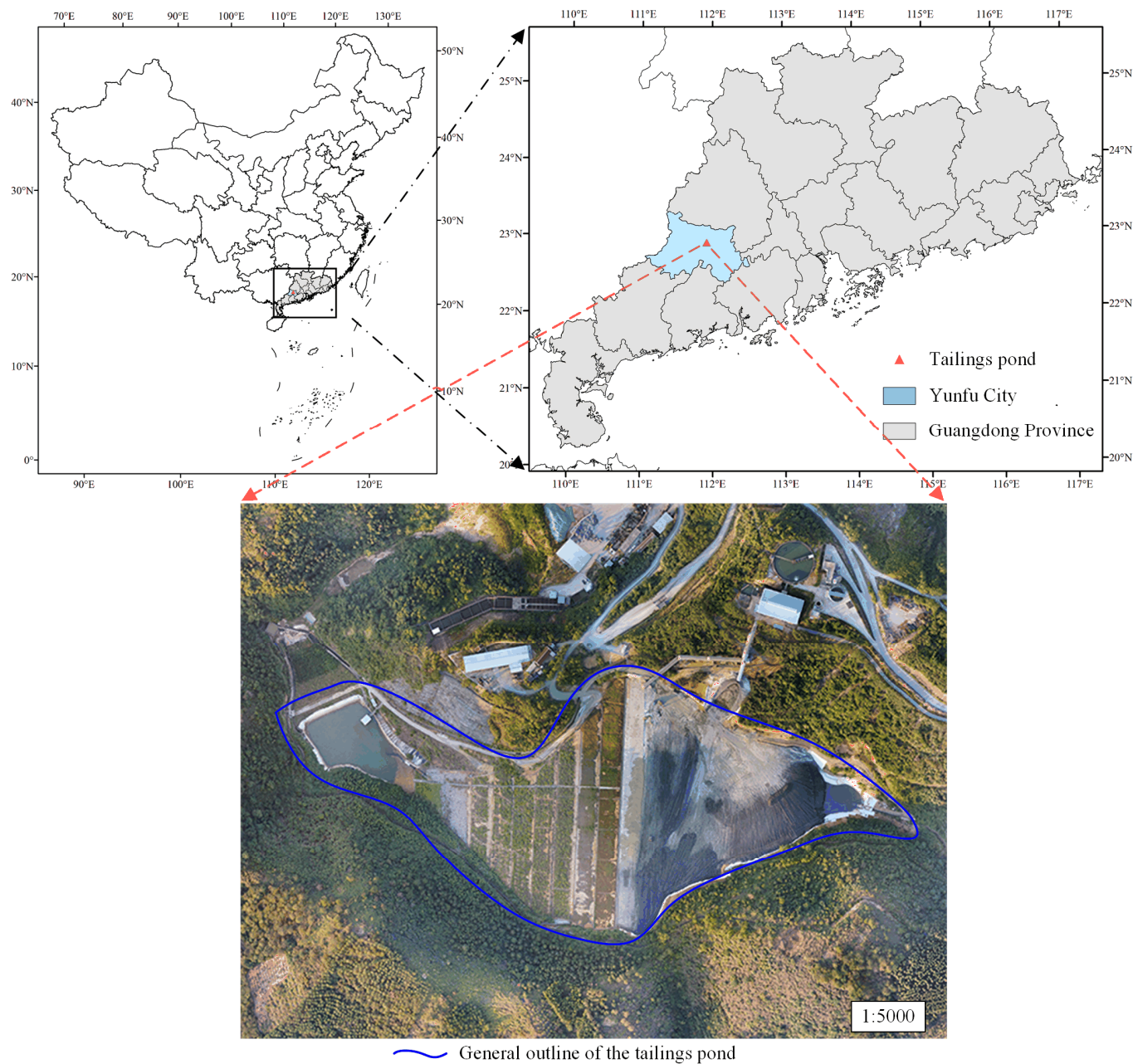


Figure 2. Location of the tailings pond.

The tailings pond was designed as a third-grade tailings pond with a designed maximum effective storage capacity and dam height of $298.93 \times 10^4 \text{ m}^3$ and 98.5 m, respectively. Currently, the tailings pond has not yet reached its final designed stage, with the current effective storage capacity and dam height at $106.06 \times 10^4 \text{ m}^3$ and 59.5 m, respectively. Based on the grading standards for tailings ponds, presented in the Supplementary Material Table S1, the tailings pond was classified as fourth grade. However, given the close proximity of its dam height to the lower limit of the third grade and the anticipated accumulation and increase in the height of the tailings dam, the grade of the tailings pond was upgraded to the third grade in this study.

2.2. Three-Dimensional (3D) Modeling with Oblique Photography and WebGIS Visualization

2.2.1. Five-Angle Oblique Photography

The UAVOP technology, which utilizes one UAV equipped with a total of five angle cameras (one vertical and four oblique angles), enables simultaneous capture of high-resolution texture images from multiple angles at the same location [45]. To prepare for the design of flight routes for UAVOP, field surveys were conducted to understand the terrain and structures around the tailings pond, including the location and height of peaks and buildings. The finalized route design is presented in Figure 3 and consists of two routes, with the route details provided in Supplementary Material Table S2. Route I covers the tailings pond, processing plant, and surrounding mountain area, covering approximately 2.55 km^2 with a total route length of 10.80 km. Given its larger coverage area and longer route length, the Loong 2160 UAV with long endurance was selected for this route. Since the valley-type tailings pond has the terrain characteristics of high elevation around the edges and low elevation in the middle with large differences in terrain elevations, a supplementary route (route II) was designed to capture photos of the tailings pond area at lower altitudes to enhance the quality of the 3D images. Route II covered a smaller area of about 0.28 km^2 with a total route length of 2.71 km, which was flown using the DJI Mavic2 quadrotor UAV. The aforementioned two UAVs are shown in Supplementary Material Figure S1.

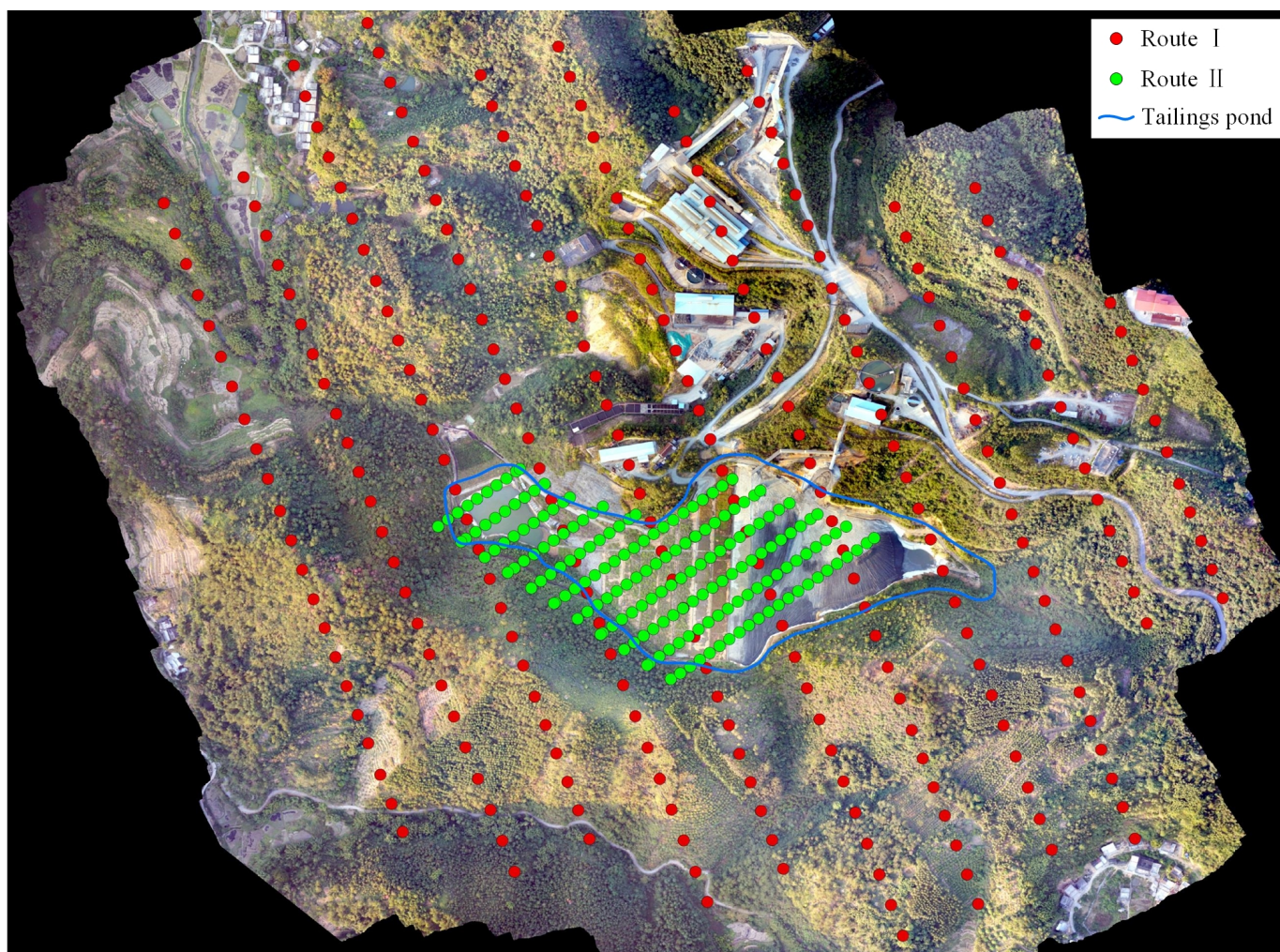


Figure 3. Designed flight route of oblique photography.

Ground control points (GCPs) are ground feature points with known geographic coordinates that are used to provide precise georeferencing and accurate 3D reconstruction

during UAV tilt photography. In this study, the selection of GCPs adhered to discerning principles such as flat terrain, open field of view, evident markers, ease of identification, and relatively uniform spatial distribution [46,47]. A total of ten GCPs were strategically deployed and measured to guarantee and improve the accuracy of the 3D images of the tailings pond. These points included six control points (numbered KZ) and four checkpoints (numbered JC), whose coordinate values and specific distribution were shown in Supplementary Material Table S3 and Figure S2, respectively. After the completion of route design and control point deployment, the UAV flight operations were conducted along the designed route under sunny and light or calm wind conditions. During the operations, the UAV automatically and synchronously transmitted the photos and position and orientation system (POS) data to the control platform. Two phases of flight operations were conducted on 8 December 2021 and 3 January 2023, respectively, and the flight operation results are shown in Supplementary Material Table S4.

2.2.2. Three-Dimensional Modeling

Two mainstream software programs of Metashape version 1.5.4 and ContextCapture version 4.4.12 for real-scene 3D modeling were used to generate high-quality 3D models based on images or point clouds. Given that Metashape performs well in aerotriangulation processing, while ContextCapture has the advantages of simple cluster production and a rich variety of result types, this study adopts a joint approach of Metashape and ContextCapture software programs for the 3D modeling of UAVOP. The photos and POS data were first imported into a new Metashape project, aligning photos to generate sparse point clouds, and exporting the aerotriangulation block. In this step, the photos of the two aircraft sorties were matched and fused by aerial triangulation to determine the position and orientation of the UAV camera in space, thereby realizing the conversion of the photographs into a sparse point cloud with geographic coordinates and elevation information. In ContextCapture, the aforementioned block was then imported into a new project, followed by checking the image files and camera parameters. Subsequently, the control point data were imported for pricking points, enabling geometric transformation through adjustments based on disparities between control point positions in the image and their actual geographical coordinates. This procedure serves to rectify and enhance the accuracy of the imagery. Finally, a new reconstruction and production project was submitted to generate real-scene 3D models in slpk and osgb formats [48].

2.2.3. Method of Accuracy Verification

In this study, four checkpoints of the GCPs were utilized to assess the accuracy of the 3D images of the tailings pond. The actual coordinates of these four checkpoints were regarded as the true values for accuracy verification and compared with the model coordinates of the checkpoints in the 3D images generated by 3D modeling to calculate the error values. The root mean square error (RMSE) was then calculated as an evaluation index, which reflects the error accuracy. The X error ΔX , Y error ΔY , elevation error ΔZ , and plane error ΔS of each checkpoint were calculated following Equations (1)–(4), and the maximum error, minimum error, average error, and RMSE of each error were calculated. The calculation formula for the RMSE is shown in Equation (5) [27,49].

$$\Delta X_i = X_{iactual} - X_{imodel} \quad (1)$$

$$\Delta Y_i = Y_{iactual} - Y_{imodel} \quad (2)$$

$$\Delta Z_i = Z_{iactual} - Z_{imodel} \quad (3)$$

$$\Delta S_i = \sqrt{\Delta X_i^2 + \Delta Y_i^2} \quad (4)$$

$$RMSE_j = \sqrt{\frac{\sum_1^n \Delta_j^2}{n}} \quad (5)$$

where i is one of the four checkpoints (JC1, JC2, JC3, or JC4); X_{actual} , Y_{actual} , and Z_{actual} are the actual coordinates (X, Y, and Z axes) of checkpoints; X_{model} , Y_{model} , and Z_{model} are the coordinates (X, Y, and Z axes) of checkpoints measured on 3D images; $RMSE$ is the root mean square error; j is one of the errors (ΔX , ΔY , ΔZ , or ΔS); and n is the total number of checkpoints.

2.2.4. WebGIS-Based 3D Visualization

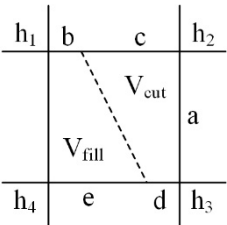
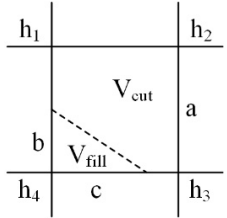
The ArcGIS Enterprise version 10.7 [50], a GIS platform software program, was utilized in this study to establish the B/S-architecture 3D image visualization and analysis function of the tailings pond, which consisted of two parts: the service layer and the application layer. The service layer included ArcGIS Portal version 10.7 and ArcGIS Pro version 2.4. The slpk-format 3D model results generated by UAVOP were uploaded to the ArcGIS Portal platform through ArcGIS Pro software version 2.4 and published as 3D services to provide the service interface of the Scene Layer for the application layer [51]. The application layer was developed based on front-end HTML5+Vue2.js technology and utilized ArcGIS API for JavaScript version 4.20 to call the interface functions on ArcGIS Portal to load 3D image services and spatial analysis services, including the 3D image visualization display, spatial geometry measurement, and other functions [52,53]. Although the ArcGIS API for JavaScript did not provide a direct interface for volume measurement, we developed a volume measurement function in conjunction with the square grid method to provide a convenience for subsequent analysis of storage capacity change and dam failure risk.

The square grid method is a technique for measuring the fill and cut of an area by dividing it into small, equal-sized squares. The volumes of fill and cut in each square are then calculated by comparing the elevation difference between each vertex and the reference plane. Finally, the total amount of fill and cut in the measurement area is obtained by summing up the fill and cut of all small squares. The smaller the square's side length, the more accurately the terrain is restored, but the workload also increases. When calculating the fill and cut, different types of vertex configurations should be considered, such as four-point all-cut (or four-point all-fill), two-fill and two-cut, and one-fill and three-cut (or one-cut and three-fill). The corresponding calculation methods are shown in Table 1. In the WebGIS volume measurement function, when there is a large number of square grids, the data interface transmission and front-end page rendering are under great pressure. In this study, data merging is performed to optimize the data interface transmission and front-end rendering time when calculating the volume of each small square grid, so as to improve the user experience.

Table 1. Calculation method of the square grid method.

Square Type	Illustrations	Calculation Formulas
Four-point all-cut (or four-point all-fill)	<p>The diagram shows a square divided into four quadrants by diagonals. Vertices are labeled h1 (top-left), h2 (top-right), h3 (bottom-right), and h4 (bottom-left). The center of the square is labeled V_{cut} (or V_{fill}). The side length of the square is labeled a.</p>	$V_{cut} (\text{or } V_{fill}) = \frac{a^2}{4} (h_1 + h_2 + h_3 + h_4)$

Table 1. Cont.

Square Type	Illustrations	Calculation Formulas
Two-fill and two-cut		$V_{cut} = \frac{a}{8}(c+d)(h_2 + h_3)$ $V_{fill} = \frac{a}{8}(b+e)(h_1 + h_4)$
One-fill and three-cut (or one-cut and three-fill)		$V_{cut} = (a^2 - \frac{bc}{2}) \frac{h_1+h_2+h_3}{5}$ $V_{fill} = \frac{bch_4}{6}$ <p>(Exchange the formulas of V_{cut} and V_{fill} when one-cut and three-fill)</p>

Notes: h_1, h_2, h_3 , and h_4 are the elevation differences between the four vertices and the reference plane, a is the side length of the square, V_{cut} is the cutting volume, and V_{fill} is the filling volume.

2.3. Analysis Method of Storage Capacity Change

Volume measurement based on UAV 3D images typically exhibited a relative error level within 10% [18,25,27,33,54,55], which indicated that the measurement technique using UAV 3D images was sufficiently reliable and could be effectively employed for volume estimation purposes. The WebGIS volume measurement function was utilized on two phases of 3D images of the tailings pond to measure and analyze the changes in storage capacity during different aerial photography periods, as illustrated in Figure 4. Initially, the fill area of the tailings pond was mapped, and the storage capacities (fill volumes) of the reservoir surface were measured using the same reference plane in both phases. The difference in storage capacity between phases I and II was then calculated to analyze the change in storage capacity during the two aerial photography periods [56]. To ensure the accuracy of the measurement outcomes, they were compared with those obtained from two mainstream 3D image viewing software, namely ContextCapture Viewer [40] and DasViewer version 3.0.2 [57].

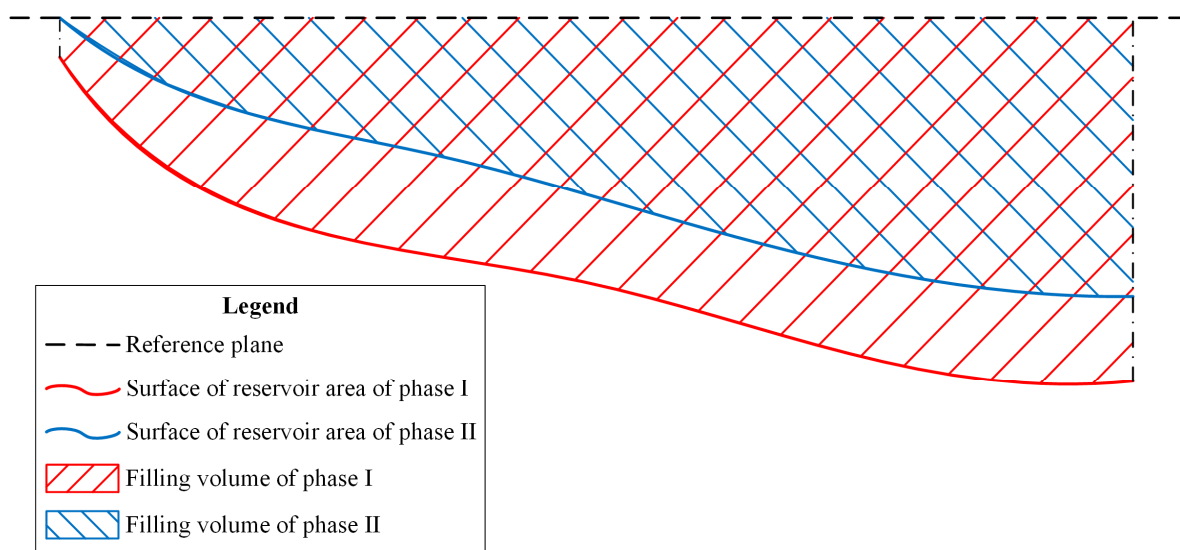


Figure 4. Analysis schematic diagram of the storage capacity change during different aerial photography periods.

2.4. Analysis Method of Dam Failure Risk

Minimum flood control dam width, minimum free height, and dam slope ratio are three pivotal parameters employed in the evaluation of dam overtopping failure risk for tailings ponds. These parameters are distinctly defined in the Safety Regulation for Tailings Pond (GB 39496-2020) [58], as provided in Supplementary Material Table S6. As shown in Figure 5, the minimum flood control dam width signifies the shortest horizontal distance (B) between the flood regulation water level and the intersection of the outer slope of the dam. The minimum free height signifies the minimum vertical difference (H_1) between the flood regulation water level and the dam top, and the dam slope ratio corresponds to the ratio ($I = L/H$) of the vertical distance (L) to the horizontal distance (H) of the tailings dam.

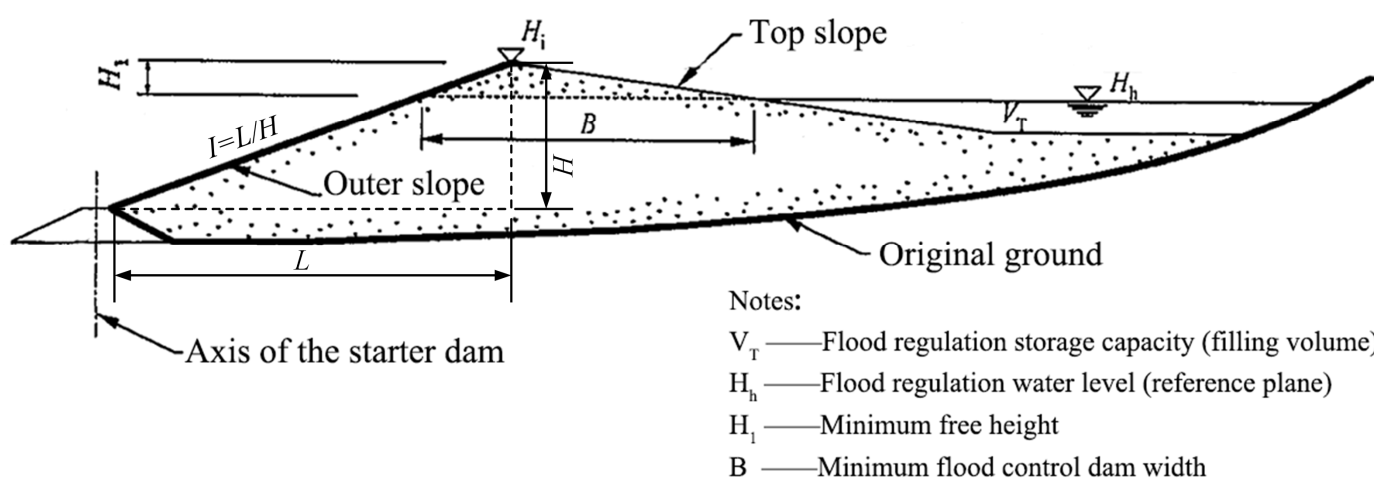


Figure 5. Schematic diagram of the dam failure risk assessment of the dry tailings pond.

In this study, the simplified flood regulation calculation method detailed in Supplementary Material Text S1 was harnessed to deduce the requisite flood regulation storage capacity for the tailings pond during the flood season. Furthermore, the WebGIS-based volume measurement function was used to determine the elevation of the flood regulation water level of the tailings pond. Initially, a reference plane was set in the fill area of the tailings pond, and the fill volume under the reference plane was measured using the volume measurement function. The reference plane was considered as the flood regulation water level (H_h) when the fill volume was equal to or slightly larger than the flood regulation storage capacity (V_T). Once the elevation of flood regulation water level was determined, the minimum flood control dam width (B) and minimum free height (H_1) of the tailings pond were measured using the WebGIS distance measurement function, to determine whether they met the requirements of flood control standards. Finally, the vertical and horizontal distances of the tailings dam were measured via the WebGIS distance measurement function, thereby deriving the dam slope ratio.

3. Results and Discussion

3.1. Accuracy Verification of 3D Images

In this study, a total of four tailings pond real-scene 3D images were generated in two phases, where each phase included one slpk-format image and one osgb-format image. The panorama images of the tailings pond 3D images are shown in Figure 6, encompassing the primary area of the tailings pond (depicted by the blue line area in the figure, the area for subsequent analysis), the mining plant (depicted by the red line area in the figure), as well as the surrounding mountainous region. It can be observed from the figure that the 3D images of the tailings pond were relatively comprehensive and clear in texture. A few voids were observed at the boundaries of the images, which resulted from insufficient aerial photographs during the oblique photography process. However, these voids were

situated in non-critical areas of the tailings pond. Figure 7 illustrates the local enlarged 3D images of the primary area of the tailings pond, offering a clear depiction of the landfill storage area (depicted by the blue line area in the figure) and the tailings dam (depicted by the red line area in the figure). The 3D images exhibited fine texture details, providing a comprehensive representation of the tailings pond. Additionally, it is evident from the blue-shaded region in the illustration that the tailings storage area has undergone obvious geomorphological changes between phases 1 and 2, marked by the deposition of numerous new tailings. The configuration of the newest layer of the tailings dam has also begun to materialize, but it has not yet been planted and greened.

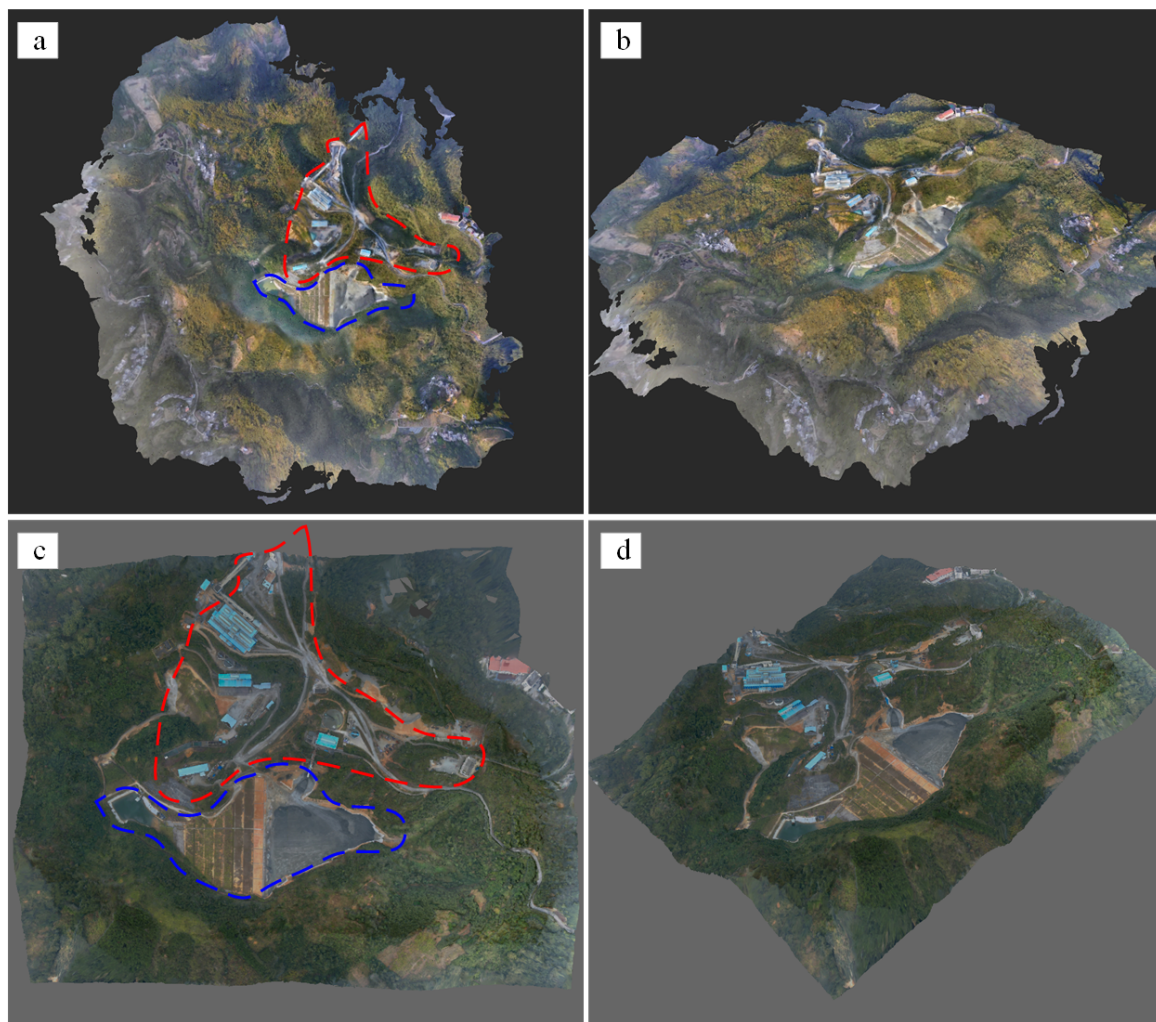


Figure 6. Panorama images of the tailings pond 3D images: (a) top view of phase I, (b) side view of phase I, (c) top view of phase II, and (d) side view of phase II. The blue dotted line shows the tailings pond area and the red dotted line shows the mining plant area.

The model coordinate values of the four checkpoints extracted from the two-phase 3D images are presented in Supplementary Material Table S7. Supplementary Material Table S8 provides a comprehensive summary of the error calibration results of the four checkpoints. The X-errors (ΔX) and Y-errors (ΔY) were below 0.20 m, the S-errors (ΔS) were below 0.25 m, and the Z-errors (ΔZ) were below 0.30 m for all four checkpoints in the two-phase 3D images. The RMSEs for the X-direction, Y-direction, plane S-direction, and elevation Z-direction of the four checkpoints in the first-phase 3D image were 0.094 m, 0.163 m, 0.188 m, and 0.198 m, respectively. Similarly, the RMSEs for the X-direction, Y-direction, plane S-direction, and elevation Z-direction of the four checkpoints in the second-phase 3D image were 0.069 m, 0.130 m, 0.147 m, and 0.201 m, respectively.

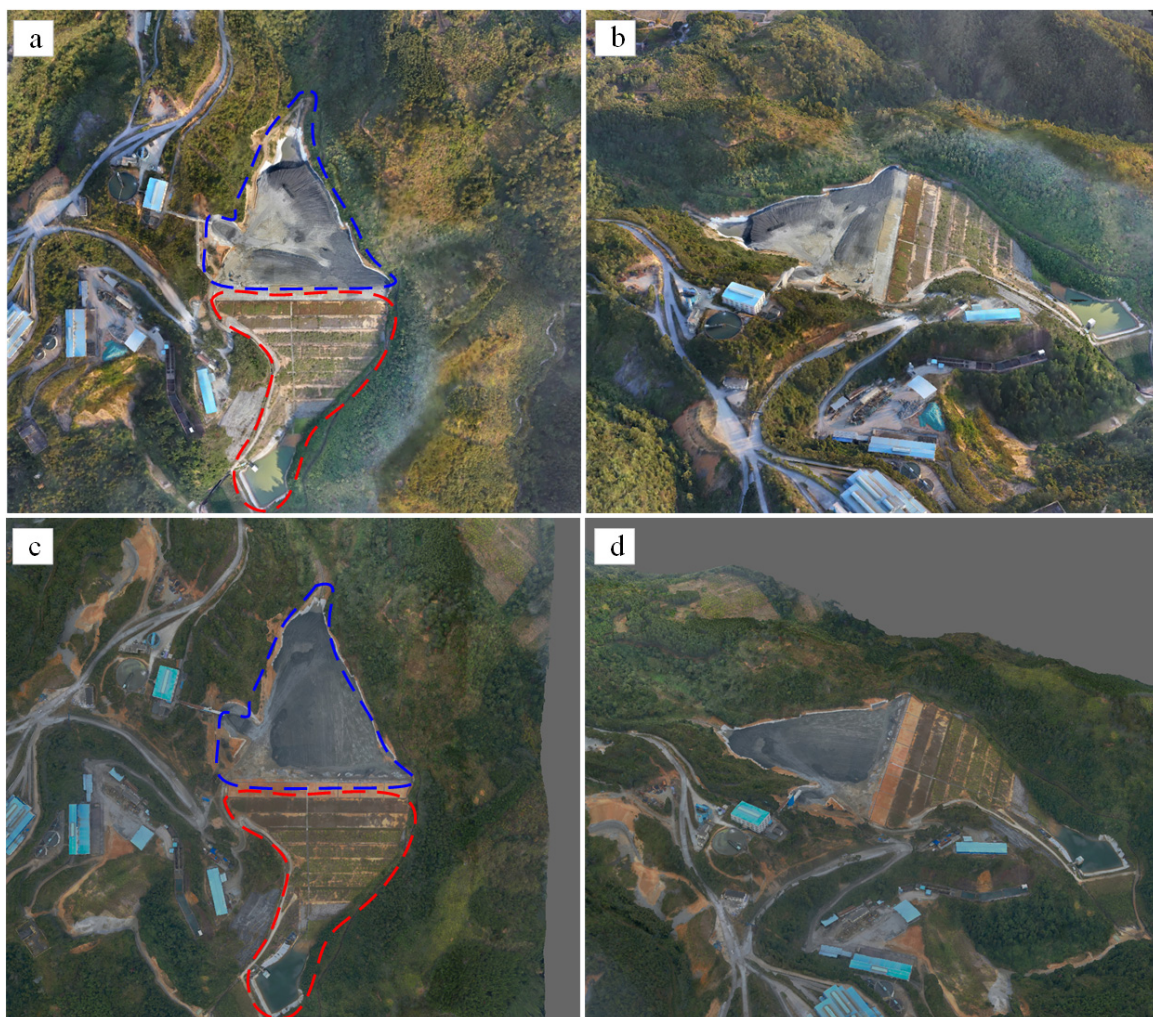


Figure 7. Local enlarged 3D images of the primary area of the tailings pond: (a) top view of phase I, (b) side view of phase I, (c) top view of phase II, and (d) side view of phase II. The blue dotted line shows the landfill storage area and the red dotted line shows the tailings dam area.

According to the requirements specified in the Specifications for the Digital Products of Three-dimensional Model on Geographic Information (CH/T 9015-2012) [59] for a level I accuracy at a mapping scale of 1:500, the plane errors of the 3D model should not exceed 0.30 m and the elevation errors should not exceed 0.37 m. The accuracy analysis results for the plane errors and elevation errors of the two phases of the tailings pond 3D images are presented in Figure 8, illustrating that both the plane errors and elevation errors of the two-phase tailings pond 3D images fell within the specified range of 0.30 m and 0.37 m, respectively. It could be concluded that the plane errors and elevation errors of the two-phase tailings pond 3D images satisfied the accuracy requirements outlined in the specification.

The existing literature on the precision of UAV-generated 3D images of tailings ponds is relatively limited, with two analogous studies outlined in Table 2. The errors observed in the 3D models generated in our study were in line with those of the other two studies, albeit slightly larger. One contributing factor to this phenomenon is that UAV oblique photography tends to exhibit notable errors when deployed in regions characterized by intricate topography and substantial elevation variations [18]. Our study site encompasses a valley-type tailings pond characterized by a significant variation in elevation, in contrast to the predominantly level and open areas considered in the other two studies. This inherent topographical disparity could plausibly contribute to the relatively slight diminution

in modeling accuracy observed in our research. Overall, the generated 3D images of the tailings pond effectively depicted the actual conditions of the tailings pond and can be utilized for subsequent analysis of storage capacity changes and dam failure risk.

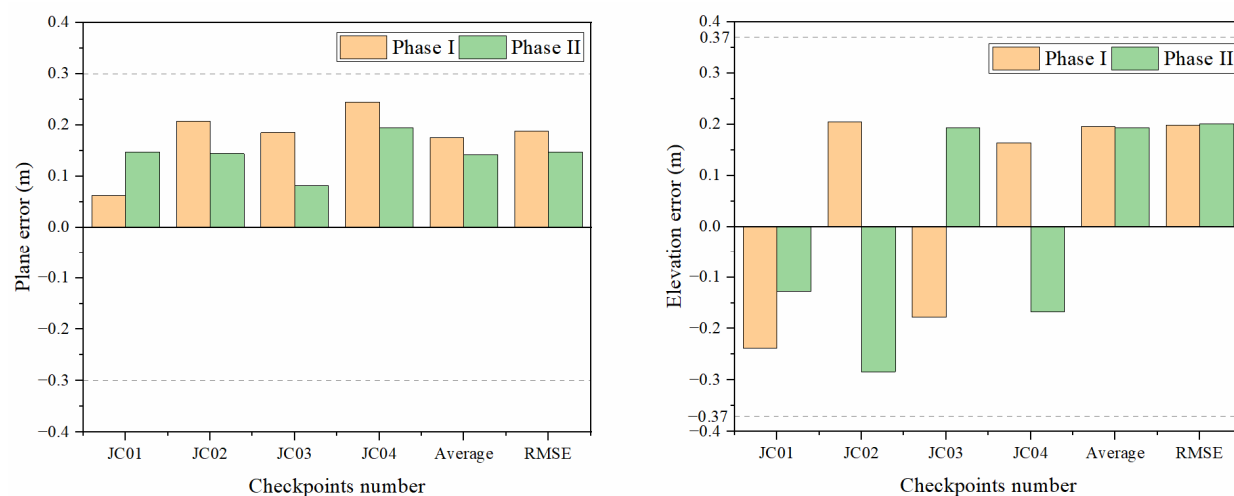


Figure 8. Accuracy analysis results for the plane errors and elevation errors of the two phases of the tailings pond 3D images.

Table 2. Three-dimensional image errors in other research.

Research	Plane Error (m)	Elevation Error
Kim et al. [30]	0.085–0.091	0.121–0.128
Mello et al. [27]	0.073–0.100	0.086–0.128

3.2. Analysis of Storage Capacity Change

The measurement results of storage capacity (fill volume) based on the WebGIS volume measurement function for the 3D images of phase I and phase II tailings ponds are shown in Supplementary Material Figure S3. The sampling distance was set at 1m, and the height of the reference plane was set at 192.50 m, corresponding to the highest elevation on the storage area of the tailings pond during both phases. Table 3 provides a summary of the WebGIS measurement results of the storage capacity change for the two phases, along with comparisons with the measurements obtained from ContextCapture Viewer and DasViewer (the measurements of both software programs are shown in Supplementary Material Figure S4). For the phase I tailings pond 3D image, the storage capacity measured by the WebGIS volume measurement function was 204,798.63 m³, while the average storage capacity measured by both software programs was 203,280.98 m³, resulting in a percentage error of 0.75%. Similarly, for the phase II tailings pond 3D image, the storage capacity measured by the WebGIS volume measurement function was 148,767.12 m³, with an average storage capacity measured by both software of 148,291.27 m³, resulting in a percentage error of 0.32%. The storage capacity change in the tailings pond, as measured by the WebGIS volume measurement function, was 148,767.12 m³, while the average storage capacity change measured by both software was 148,291.27 m³, resulting in a percentage error of 0.32%. All of these percentage errors satisfied the requirements of the Code for Urban Survey (CJJ/T 8-2011) [60] for the percentage errors of the two earthwork volumes to be less than 3%. Therefore, it can be concluded that the storage capacity change measurements obtained using the WebGIS volume measurement function were relatively reliable. The storage capacity change in this tailings pond during the two aerial photography periods was estimated to be approximately 56,031.51 m³.

Table 3. Summary results of measuring storage capacity change.

Phase	Storage Capacity by WebGIS Measurement (m^3)	Storage Capacity by Both Software (m^3)			Percentage Error (%)
		ContextCapture Viewer	DasViewer	Average	
I	204,798.63	203,144.91	203,417.05	203,280.98	0.75
II	148,767.12	148,182.43	148,400.10	148,291.27	0.32
Change	56,031.51	54,962.48	55,016.95	54,989.71	1.89

Due to the hazardous limitations of the tailings pond stack site, it is difficult for the traditional manual geodetic measurement method to approach each place of the tailings pond to measure the storage capacity change. Based on UAVOP, it is possible to obtain the ground geographic information of the whole tailings pond, so that the storage capacity change data of the tailings pond can be obtained in a more comprehensive and convenient way. Meanwhile, the reliability of the volume measurement based on UAV 3D images has also been confirmed in related research [18,25,27,33,54,55]. In addition, the WebGIS UAV 3D images can be more conveniently and easily shared with users to improve user-friendliness.

3.3. Analysis of Dam Failure Risk

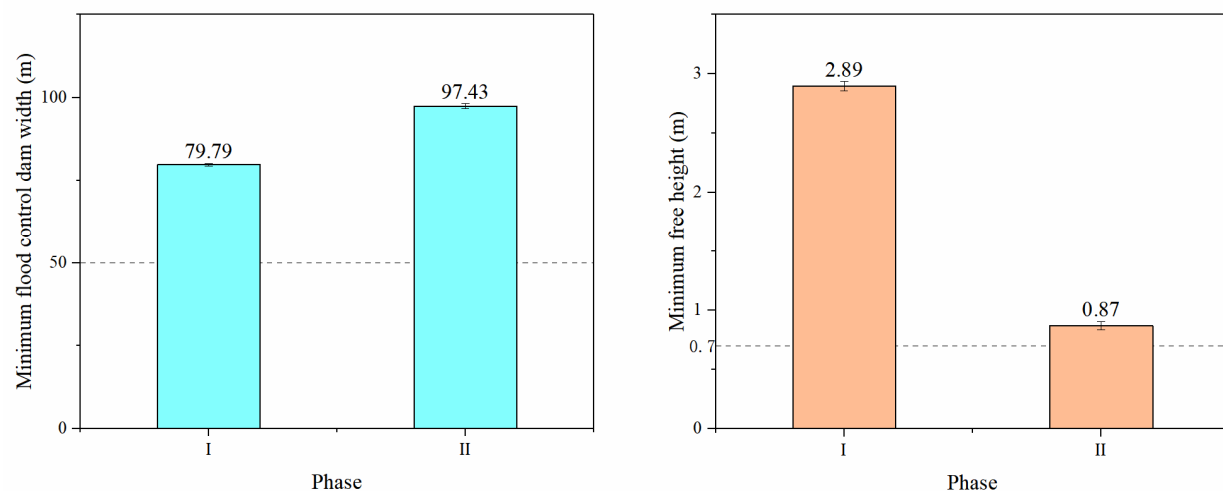
Supplementary Material Table S9 provides the parameters relevant to the calculation of design rainstorm intensity [61]. The catchment area (F) and the maximum flood discharge capacity (q_m) of the tailings pond were 0.19 km^2 and $8.35 \text{ m}^3/\text{s}$, respectively. The flood regulation calculation results, as per the methodology described in Supplementary Material Text S1, are summarized in Supplementary Material Table S10. For a 200-year flood control standard, the total catchment flood amount for a rainfall duration of 24 h (W_{24P}) was $85,196.00 \text{ m}^3$, the flood peak flow (Q_p) was $12.28 \text{ m}^3/\text{s}$, and the required flood regulation storage capacity (V_T) was determined to be $38,644.48 \text{ m}^3$.

The measurement results of the flood regulation water level of the two phases of the tailings pond based on the WebGIS volume measurement function are shown in Supplementary Material Figure S5, with the sampling distance set to 1 m. In the figure, the blue (fill) areas represented the requested flood regulation storage capacity, while the difference in the red (cut) areas did not impact the measurement results. Table 4 provides a summary of the WebGIS measurement results of the flood regulation water level for the two phases, along with comparisons with the measurements obtained from the ContextCapture Viewer and DasViewer (the measurements of both software programs were as shown in Supplementary Material Figure S6). For the 3D image of the phase I tailings pond, the flood regulation water level determined using the WebGIS volume measurement function was found to be 185.24 m, corresponding to a fill volume of $37,889.80 \text{ m}^3$. The average fill volume measured by both software programs was $38,078.01 \text{ m}^3$, with a percentage error of -0.49% compared to the WebGIS measurement. Similarly, for the 3D image of the phase II tailings pond, the flood regulation water level determined using the WebGIS volume measurement function was found to be 188.79 m, corresponding to a fill volume of $37,878.31 \text{ m}^3$. The average fill volume measured by both software programs was $37,793.18 \text{ m}^3$, with a percentage error of 0.23% compared to the WebGIS measurement. Both aforementioned percentage errors satisfied the requirements of the Code for Urban Survey (CJJ/T 8-2011) for the percentage errors of the two earthwork volumes to be less than 3%. Thus, it can be concluded that the flood regulation water level measurements obtained using the WebGIS volume measurement function were relatively reliable, and the flood regulation water levels of the tailings pond were determined to be 185.24 m and 188.79 m for phases I and II, respectively.

Table 4. Summary results of measuring flood regulation water level.

Phase	Flood Regulation Water Level (m)	Fill Volume by WebGIS Measurement (m^3)	Fill Volume by Both Software (m^3)			Percentage Error (%)
			ContextCapture Viewer	DasViewer	Average	
I	185.24	37,889.80	38,060.67	38,095.34	38,078.01	-0.49
II	188.79	37,878.31	37,786.00	37,800.36	37,793.18	0.23

Upon determining the flood regulation water levels, the WebGIS distance measurement function was employed to rapidly measure the minimum flood control dam width and the minimum free height, two key parameters related to the risk of dam failure, for both phases of the tailings pond. To minimize errors, two parameters were measured five times for each phase and averaged. The measurement results are presented in Supplementary Material Table S11 and Figure 9. The phase I tailings pond exhibited a minimum flood control dam width of 79.79 m and a minimum free height of 2.89 m, while the phase II tailings pond displayed a minimum flood control dam width of 97.43 m and a minimum free height of 0.87 m. The standard deviations (SD) of the above measurements are all relatively small, which underscores the relative reliability and accuracy of the measurement results. Furthermore, both phases of the tailings pond demonstrated minimum flood control dam widths and minimum free heights exceeding the corresponding thresholds of 50 m and 0.7 m specified for third-grade tailings ponds in Supplementary Material Table S6, which satisfied the flood control standard outlined in the Safety Regulation for Tailings Pond (GB 39496-2020).

**Figure 9.** Minimum flood control dam widths and minimum free heights of the two phases of the tailings pond 3D images.

Additionally, in this study, the measurements of dam slope ratios were conducted by extracting five slopes from each of the two tailings dams using the WebGIS distance measurement function. As demonstrated in the provided table (Table 5), the measured dam slope ratios for the tailings ponds in phase I and phase II were 1:4.05 and 1:4.14, respectively. It is worth noting that the marginal disparity in the measured slope ratios between the two phases may be attributed to potential measurement inaccuracies stemming from the newly constructed layer of tailings dams between the two phases. Nevertheless, in general, the dam slope ratios for both phases approximate each other closely, hovering around 1:4. These outcomes satisfied the stipulated criterion of a slope ratio lower than 1:3, as prescribed by the requirements in the Safety Regulation for Tailings Pond (GB 39496-2020). This indicated a relatively favorable stability status of the tailings dam with a correspondingly low likelihood of dam failure.

Table 5. The summary results of measuring flood regulation water level.

Number	Phase I			Phase II		
	H	L	Dam Slope Ratio	H	L	Dam Slope Ratio
1	38.39	156.24	1:4.07	39.69	164.25	1:4.14
2	37.80	153.58	1:4.06	39.52	164.34	1:4.16
3	32.46	131.19	1:4.04	34.03	140.61	1:4.13
4	24.02	97.74	1:4.07	24.62	102.45	1:4.16
5	18.66	75.06	1:4.02	19.68	80.8	1:4.11
Average	/	/	1:4.05	/	/	1:4.14

To recapitulate, the minimum flood control dam widths, minimum free heights, and dam slope ratios for both phases of this tailings pond adhere to the prescribed standard specifications. These outcomes implied that the tailings pond demonstrated a favorable operational condition during these two time periods. Therefore, under the present operating conditions, the tailings pond was capable of effectively withstanding a major flood with a recurrence period of 200 years, and the risk of flood topping and dam failure was low. Moreover, it is worth noting that the minimum flood control dam width has increased from 79.79 m to 97.43 m, while the minimum free height has decreased from 2.89 m to 0.87 m. Although the minimum free height in phase II still complied with the requirements, it was in close proximity to the standard specified threshold of 0.7 m. Tailings pond enterprises and supervisory authorities should consider remaining vigilant regarding the flood level and minimum free height of the tailings pond to prevent occurrences of flood overtopping and potential dam failure.

4. Conclusions

In this study, an innovative WebGIS-based UAVOP method has been developed to analyze the storage capacity change and dam failure risk for tailings ponds. The applicability of this innovative approach was then validated by deploying it to perform rapid measurement and analysis of the storage capacity change and compliance with key parameters related to dam overtopping failure risk at a tailings pond in Yunfu City, Guangdong Province, China. Compared to the conventional methods, this approach provides the advantages of timeliness, flexibility, and relatively low costs. The constructing and visualizing real-scene 3D images of the tailings pond were performed in two phases, with the RMSEs of plane errors and elevation errors at 0.188 m and 0.198 m for phase I, and 0.147 m and 0.201 m for phase II, respectively. It was verified that the 3D images for both phases satisfied the specified accuracy requirements, which can be used for the subsequent measurement analysis related to storage capacity change and dam failure risk of the tailings pond. The analysis showed that the storage capacities of phase I and phase II of the tailings pond were measured to be 204,798.63 m³ and 148,291.27 m³, respectively, with a storage capacity change of 56,031.51 m³. In addition, for phase I, the minimum flood control dam width, minimum free height, and dam slope ratio were measured at 79.60 m, 2.92 m, and 1:4.05, respectively, while for phase II, these values were 97.35 m, 0.88 m, and 1:4.14, respectively. These parameters associated with the dam failure risk in both phases complied with the flood control requirements for a third-grade tailings pond, indicating a low risk of dam failure in the tailings pond.

However, there were still two limitations in our study. First, the tailings dam risk assessment method employed in this study is based on specific technical standards in China, which is not a globally applicable standard. In order to ensure the accuracy and applicability of the assessment results when applying this method to other countries, referencing the corresponding local technical standards is recommended. Second, this study did not account for the potential impact of vegetation and obscured areas on the tailings pond's surface when determining the volume measurement results. Subsequent

studies may consider in-depth optimization of the 3D image or volume measurement functions to enhance the precision of tailings pond volume change measurements.

Overall, the reported approach of WebGIS-based UAVOP technology was demonstrated to provide high-resolution 3D images and realize visualization displays of tailings ponds, which enhances the efficiency of measurement of storage capacity changes and key parameters associated with the dam failure risk for tailings ponds. This advanced technology provides a new and efficient technical solution for analyzing storage capacity changes and assessing dam failure risks in tailings ponds with similar structures all over the world. Moreover, this approach can also be used for similar applications in other solid waste or landfill volume-related monitoring.

Supplementary Materials: The following supporting information can be downloaded at: <https://www.mdpi.com/article/10.3390/su151914062/s1>, Text S1: calculation method of flood regulation storage capacity; Table S1: grading standards for tailings ponds; Table S2: detailed parameters of UAV flight route; Table S3: GSPs data; Table S4: results of two phases of flight operations; Table S5: flood control standards for tailings ponds; Table S6: requirements for minimum flood control dam width and minimum free height of dry tailings pond dams; Table S7: model coordinates of the four checkpoints; Table S8: comprehensive summary of the error calibration results of the four checkpoints; Table S9: calculation parameters of design rainstorm intensity; Table S10: calculation results of flood regulation storage capacity; Table S11: summary results of measuring minimum flood control dam width and minimum free height; Figure S1: UAVs; Figure S2: location distribution of GCPs; Figure S3: measured results of storage capacity based on WebGIS volume measurement function; Figure S4: measured results of storage capacity based on two software; Figure S5: measured results of flood regulation water level based on WebGIS volume measurement function; Figure S6: measured results of flood regulation water level based on two software.

Author Contributions: Conceptualization, M.Z.; methodology, M.Z.; validation, Y.Y.; formal analysis, Y.Y.; investigation, M.Z.; resources, Y.Z. and J.-C.J.; data curation, Y.Z. and J.-C.J.; writing—original draft preparation, M.Z.; writing—review and editing, Y.Z., J.-C.J., S.W., P.-C.C., C.S., S.L. and Y.L.; visualization, Y.Y.; supervision, Y.Z. and J.-C.J.; project administration, Y.Z.; funding acquisition, Y.Z. All authors have read and agreed to the published version of the manuscript.

Funding: This research was funded by the High-end Foreign Experts Recruitment Plan (Grant No. G2023163014L).

Institutional Review Board Statement: Not applicable.

Informed Consent Statement: Not applicable.

Data Availability Statement: Not applicable.

Conflicts of Interest: The authors declare no conflict of interest.

References

1. Dong, L.J.; Deng, S.J.; Wang, F.Y. Some developments and new insights for environmental sustainability and disaster control of tailings dam. *J. Clean. Prod.* **2020**, *269*, 122270. [[CrossRef](#)]
2. Wan, Y.T.; Zhong, Y.F.; Ma, A.L.; Hu, X.; Wei, L.F. Satellite-air-ground integrated multi-source earth observation and machine learning processing brain for tailings reservoir monitoring and rapid emergency response. *Land. Degrad. Dev.* **2023**, *34*, 1941–1959. [[CrossRef](#)]
3. Du, Z.Y.; Ge, L.L.; Ng, A.H.M.; Zhu, Q.G.Z.; Horgan, F.G.; Zhang, Q. Risk assessment for tailings dams in Brumadinho of Brazil using InSAR time series approach. *Sci. Total Environ.* **2020**, *717*, 137125. [[CrossRef](#)] [[PubMed](#)]
4. Lyu, J.; Hu, Y.; Ren, S.; Yao, Y.; Ding, D.; Guan, Q.; Tao, L. Extracting the Tailings Ponds from High Spatial Resolution Remote Sensing Images by Integrating a Deep Learning-Based Model. *Remote Sens.* **2021**, *13*, 743. [[CrossRef](#)]
5. Cacciuttolo, C.; Cano, D. Spatial and Temporal Study of Supernatant Process Water Pond in Tailings Storage Facilities: Use of Remote Sensing Techniques for Preventing Mine Tailings Dam Failures. *Sustainability* **2023**, *15*, 4984. [[CrossRef](#)]
6. Burritt, R.L.; Christ, K.L. Full cost accounting: A missing consideration in global tailings dam management. *J. Clean. Prod.* **2021**, *321*, 129016. [[CrossRef](#)]
7. Owen, J.R.; Kemp, D.; Lebre, E.; Svobodova, K.; Murillo, G.P. Catastrophic tailings dam failures and disaster risk disclosure. *Int. J. Disaster Risk Reduct.* **2020**, *42*, 101361. [[CrossRef](#)]

8. Lumbroso, D.; McElroy, C.; Goff, C.; Collell, M.R.; Petkovsek, G.; Wetton, M. The potential to reduce the risks posed by tailings dams using satellite-based information. *Int. J. Disaster Risk Reduct.* **2019**, *38*, 101209. [[CrossRef](#)]
9. Liu, J.; Liu, R.; Zhang, Z.; Cai, Y.; Zhang, L. A Bayesian Network-based risk dynamic simulation model for accidental water pollution discharge of mine tailings ponds at watershed-scale. *J. Environ. Manag.* **2019**, *246*, 821–831. [[CrossRef](#)]
10. Lin, S.-Q.; Wang, G.-J.; Liu, W.-L.; Zhao, B.; Shen, Y.-M.; Wang, M.-L.; Li, X.-S. Regional Distribution and Causes of Global Mine Tailings Dam Failures. *Metals* **2022**, *12*, 905. [[CrossRef](#)]
11. Hancock, G.R.; Coulthard, T.J. Tailings dams: Assessing the long-term erosional stability of valley fill designs. *Sci. Total Environ.* **2022**, *849*, 157692. [[CrossRef](#)] [[PubMed](#)]
12. Guimaraes, R.N.; Moreira, V.R.; Marciano de Oliveira, L.V.; Amaral, M.C.S. A conceptual model to establish preventive and corrective actions to guarantee water safety following scenarios of tailing dam failure. *J. Environ. Manag.* **2023**, *344*, 118506. [[CrossRef](#)] [[PubMed](#)]
13. Cacciuttolo, C.; Cano, D. Environmental Impact Assessment of Mine Tailings Spill Considering Metallurgical Processes of Gold and Copper Mining: Case Studies in the Andean Countries of Chile and Peru. *Water* **2022**, *14*, 3057. [[CrossRef](#)]
14. Petkovsek, G.; Hassan, M.; Lumbroso, D.; Collell, M.R. A Two-Fluid Simulation of Tailings Dam Breaching. *Mine Water Environ.* **2021**, *40*, 151–165. [[CrossRef](#)]
15. Piciullo, L.; Storosten, E.B.; Liu, Z.Q.; Nadim, F.; Lacasse, S. A new look at the statistics of tailings dam failures. *Eng. Geol.* **2022**, *303*, 106657. [[CrossRef](#)]
16. Wu, P.; Liang, B.; Jin, J.; Zhou, K.; Guo, B.; Yang, Z. Solution and Stability Analysis of Sliding Surface of Tailings Pond under Rainstorm. *Sustainability* **2022**, *14*, 3081. [[CrossRef](#)]
17. Wang, G.J.; Zhao, B.; Lan, R.; Liu, D.W.; Wu, B.S.; Li, Y.J.; Li, Q.M.; Zhou, H.M.; Liu, M.S.; Liu, W.L.; et al. Experimental Study on Failure Model of Tailing Dam Overtopping under Heavy Rainfall. *Lithosphere* **2022**, *2022*, 5922501. [[CrossRef](#)]
18. Filkin, T.; Sliusar, N.; Huber-Humer, M.; Ritzkowski, M.; Korotaev, V. Estimation of dump and landfill waste volumes using unmanned aerial systems. *Waste Manag.* **2022**, *139*, 301–308. [[CrossRef](#)]
19. Yan, D.; Li, G.; Li, X.; Zhang, H.; Lei, H.; Lu, K.; Cheng, M.; Zhu, F. An Improved Faster R-CNN Method to Detect Tailings Ponds from High-Resolution Remote Sensing Images. *Remote Sens.* **2021**, *13*, 2052. [[CrossRef](#)]
20. Martinez-Segura, M.A.; Vasconez-Maza, M.D.; Garcia-Nieto, M.C. Volumetric characterisation of waste deposits generated during the production of fertiliser derived from phosphoric rock by using LiDAR and electrical resistivity tomography. *Sci. Total Environ.* **2020**, *716*, 137076. [[CrossRef](#)]
21. Martin-Velazquez, S.; Rodriguez-Santalla, I.; Ropero-Szymanska, N.; Gomez-Ortiz, D.; Martin-Crespo, T.; de Ignacio-San Jose, C. Geomorphological Mapping and Erosion of Abandoned Tailings in the Hiendelaencina Mining District (Spain) from Aerial Imagery and LiDAR Data. *Remote Sens.* **2022**, *14*, 4617. [[CrossRef](#)]
22. Martin-Crespo, T.; Gomez-Ortiz, D.; Pryimak, V.; Martin-Velazquez, S.; Rodriguez-Santalla, I.; Ropero-Szymanska, N.; de Ignacio-San Jose, C. Quantification of Pollutants in Mining Ponds Using a Combination of LiDAR and Geochemical Methods-Mining District of Hiendelaencina, Guadalajara (Spain). *Remote Sens.* **2023**, *15*, 1423. [[CrossRef](#)]
23. Ren, H.; Zhao, Y.; Xiao, W.; Wang, X.; Sui, T. An Improved Ground Control Point Configuration for Digital Surface Model Construction in a Coal Waste Dump Using an Unmanned Aerial Vehicle System. *Remote Sens.* **2020**, *12*, 1623. [[CrossRef](#)]
24. Gong, C.; Lei, S.; Bian, Z.; Liu, Y.; Zhang, Z.; Cheng, W. Analysis of the Development of an Erosion Gully in an Open-Pit Coal Mine Dump During a Winter Freeze-Thaw Cycle by Using Low-Cost UAVs. *Remote Sens.* **2019**, *11*, 1356. [[CrossRef](#)]
25. Sliusar, N.; Filkin, T.; Huber-Humer, M.; Ritzkowski, M. Drone technology in municipal solid waste management and landfilling: A comprehensive review. *Waste Manag.* **2022**, *139*, 1–16. [[CrossRef](#)] [[PubMed](#)]
26. Torok, A.; Bogoly, G.; Somogyi, A.; Lovas, T. Application of UAV in Topographic Modelling and Structural Geological Mapping of Quarries and Their Surroundings-Delineation of Fault-Bordered Raw Material Reserves. *Sensors* **2020**, *20*, 489. [[CrossRef](#)] [[PubMed](#)]
27. Mello, C.C.S.; Salim, D.H.C.; Simoes, G.F. UAV-based landfill operation monitoring: A year of volume and topographic measurements. *Waste Manag.* **2022**, *137*, 253–263. [[CrossRef](#)]
28. Johansen, K.; Erskine, P.D.; McCabe, M.F. Using Unmanned Aerial Vehicles to assess the rehabilitation performance of open cut coal mines. *J. Clean. Prod.* **2019**, *209*, 819–833. [[CrossRef](#)]
29. Wong, L.; Vien, B.S.; Ma, Y.; Kuen, T.; Courtney, F.; Kodikara, J.; Chiu, W.K. Remote Monitoring of Floating Covers Using UAV Photogrammetry. *Remote Sens.* **2020**, *12*, 1118. [[CrossRef](#)]
30. Kim, D.-P.; Kim, S.-B.; Back, K.-S. Analysis of Mine Change Using 3D Spatial Information Based on Drone Image. *Sustainability* **2022**, *14*, 3433. [[CrossRef](#)]
31. Wang, K.; Yang, P.; Yu, G.M.; Yang, C.; Zhu, L.Y. 3D Numerical Modelling of Tailings Dam Breach Run Out Flow over Complex Terrain: A Multidisciplinary Procedure. *Water* **2020**, *12*, 2538. [[CrossRef](#)]
32. Zhou, D.W.; Wang, L.; An, S.K.; Wang, X.P.; An, Y.F. Integration of unmanned aerial vehicle (UAV)-based photogrammetry and InSAR for mining subsidence and parameters inversion: A case study of the Wangjiata Mine, China. *Bull. Eng. Geol. Environ.* **2022**, *81*, 343. [[CrossRef](#)]
33. Cao, D.G.; Zhang, B.L.; Zhang, X.B.; Yin, L.; Man, X.C. Optimization methods on dynamic monitoring of mineral reserves for open pit mine based on UAV oblique photogrammetry. *Measurement* **2023**, *207*, 112364. [[CrossRef](#)]

34. Melton, C.A.; Hughes, D.C.; Page, D.L.; Phillips, M.S. Temporal multispectral and 3D analysis of Cerro de Pasco, Peru. *Sci. Total Environ.* **2020**, *706*, 135640. [CrossRef] [PubMed]
35. Luo, W.D.; Gan, S.; Yuan, X.P.; Gao, S.; Bi, R.; Hu, L. Test and Analysis of Vegetation Coverage in Open-Pit Phosphate Mining Area around Dianchi Lake Using UAV-VDVI. *Sensors* **2022**, *22*, 6388. [CrossRef]
36. Zhang, H.; Li, Q.M.; Wang, J.C.; Fu, B.T.; Duan, Z.J.; Zhao, Z.Y. Application of Space-Sky-Earth Integration Technology with UAVs in Risk Identification of Tailings Ponds. *Drones* **2023**, *7*, 222. [CrossRef]
37. Lastilla, L.; Belloni, V.; Ravanello, R.; Crespi, M. DSM Generation from Single and Cross-Sensor Multi-View Satellite Images Using the New Agisoft Metashape: The Case Studies of Trento and Matera (Italy). *Remote Sens.* **2021**, *13*, 593. [CrossRef]
38. Agisoft. Metashape. Available online: <https://www.agisoft.com/> (accessed on 1 May 2023).
39. Lewinska, P.; Glowacki, O.; Moskalik, M.; Smith, W.A.P. Evaluation of structure-from-motion for analysis of small-scale glacier dynamics. *Measurement* **2021**, *168*, 108327. [CrossRef]
40. Bentley. ContextCapture. Available online: <https://www.bentley.com/software/contextcapture/> (accessed on 1 May 2023).
41. Mazzei, M.; Quaroni, D. Development of a 3D WebGIS Application for the Visualization of Seismic Risk on Infrastructural Work. *ISPRS Int. J. Geo-Inf.* **2022**, *11*, 22. [CrossRef]
42. Liu, J.; Wang, J.; Chen, Y.; Lippold, H.; Xiao, T.; Li, H.; Shen, C.-C.; Xie, L.; Xie, X.; Yang, H. Geochemical transfer and preliminary health risk assessment of thallium in a riverine system in the Pearl River Basin, South China. *J. Geochem. Explor.* **2017**, *176*, 64–75. [CrossRef]
43. People's Government of Yunfu Yunan District. Physical Geography. Available online: https://www.yunan.gov.cn/yaqrmaf/zjya/zrdl/content/post_1274105.html (accessed on 9 February 2021).
44. Yao, C.; Wu, L.G.; Yang, J.H.; Xiao, L.X.; Liu, X.F.; Jiang, Q.H.; Zhou, C.B. Influences of Tailings Particle Size on Overtopping Tailings Dam Failures. *Mine Water Environ.* **2021**, *40*, 174–188. [CrossRef]
45. Lai, H.; Liu, L.; Liu, X.; Zhang, Y.; Xuan, X. Unmanned aerial vehicle oblique photography-based superposed fold analysis of outcrops in the Xuhuai region, North China. *Geol. J.* **2020**, *56*, 2212–2222. [CrossRef]
46. Tucci, G.; Gebbia, A.; Conti, A.; Fiorini, L.; Lubello, C. Monitoring and Computation of the Volumes of Stockpiles of Bulk Material by Means of UAV Photogrammetric Surveying. *Remote Sens.* **2019**, *11*, 1471. [CrossRef]
47. Yang, C.-J.; Yeh, L.-W.; Cheng, Y.-C.; Jen, C.-H.; Lin, J.-C. Badland Erosion and Its Morphometric Features in the Tropical Monsoon Area. *Remote Sens.* **2019**, *11*, 3051. [CrossRef]
48. Che, Y.; Wang, Q.; Xie, Z.; Zhou, L.; Li, S.; Hui, F.; Wang, X.; Li, B.; Ma, Y. Estimation of maize plant height and leaf area index dynamics using an unmanned aerial vehicle with oblique and nadir photography. *Ann. Bot.* **2020**, *126*, 765–773. [CrossRef]
49. Incekara, A.; Delen, A.; Seker, D.; Goksel, C. Investigating the Utility Potential of Low-Cost Unmanned Aerial Vehicles in the Temporal Monitoring of a Landfill. *ISPRS Int. J. Geo-Inf.* **2019**, *8*, 22. [CrossRef]
50. Esri. ArcGIS Enterprise. Available online: <https://enterprise.arcgis.com/en/> (accessed on 1 May 2023).
51. Savini, L.; Tora, S.; Di Lorenzo, A.; Cioci, D.; Monaco, F.; Polci, A.; Orsini, M.; Calistri, P.; Conte, A. A Web Geographic Information System to share data and explorative analysis tools: The application to West Nile disease in the Mediterranean basin. *PLoS ONE* **2018**, *13*, e0196429. [CrossRef]
52. Wei, L.; Hong, L.; Wenjie, X.; Xiaolin, K. A WebGIS-Based Platform for Sewage Treatment Facilities in Villages and Small Towns Near the Lake Dian. *J. Phys. Conf. Ser.* **2021**, *1961*, 012066. [CrossRef]
53. Ding, H.; Cai, M.; Lin, X.; Chen, T.; Li, L.; Liu, Y. RTVEMVS: Real-time modeling and visualization system for vehicle emissions on an urban road network. *J. Clean. Prod.* **2021**, *309*, 127166. [CrossRef]
54. Fys, M.; Yurkiv, M.; Lozynskyi, V. Modeling of 3-D objects using geodetic and cartographic data and determining their volumes with an accuracy assessment. *Remote Sens. Appl. Soc. Environ.* **2021**, *22*, 100506. [CrossRef]
55. Park, H.C.; Rachmawati, T.S.N.; Kim, S. UAV-Based High-Rise Buildings Earthwork Monitoring-A Case Study. *Sustainability* **2022**, *14*, 10179. [CrossRef]
56. Labant, S.; Gergelova, M.B.; Kuzevicova, Z.; Kuzevic, S.; Fedorko, G.; Molnar, V. Utilization of Geodetic Methods Results in Small Open-Pit Mine Conditions: A Case Study from Slovakia. *Minerals* **2020**, *10*, 489. [CrossRef]
57. Daspatial. DasViewer. Available online: <https://www.daspalatial.com/cn/dasviewer> (accessed on 1 May 2023).
58. GB 39496-2020; Safety Regulation for Tailings Pond. State Administration for Market Regulation. Standardization Administration: Beijing, China, 2020.
59. CH/T 9015-2012; Specifications for the Digital Products of Three-dimensional Model on Geographic Information. State Bureau of Surveying and Mapping: Beijing, China, 2012.
60. CJJ/T 8-2011; Code for Urban Survey. Ministry of Housing and Urban-Rural Development of the People's Republic of China: Beijing, China, 2011.
61. Guangdong Hydrological Station. *Guangdong Storm Runoff Check Calculation Chart*; Guangdong Hydrological Station: Guangzhou, China, 1991.

Disclaimer/Publisher's Note: The statements, opinions and data contained in all publications are solely those of the individual author(s) and contributor(s) and not of MDPI and/or the editor(s). MDPI and/or the editor(s) disclaim responsibility for any injury to people or property resulting from any ideas, methods, instructions or products referred to in the content.